Superconductivity in functionalized niobium-carbide MXenes

Superconductivity in functionalized niobium-carbide MXenes

Cem Sevik,[a,b,†] Jonas Bekaert,[a,†] and Milorad V. Milošević[a]

We detail the effects of Cl and S functionalization on the superconducting properties of layered (bulk) and monolayer niobium carbide (Nb_2C) MXene crystals, based on first-principles calculations combined with Eliashberg theory. For the bulk layered Nb_2CCl_2, the calculated superconducting transition temperature (T_c) is in very good agreement with the recently measured value of 6 K. We show that T_c is enhanced to 10 K for monolayer Nb_2CCl_2, due to an increase in the density of states at the Fermi level, and the corresponding electron-phonon coupling. We further demonstrate feasible gate- and strain-induced enhancements of T_c for both bulk-layered and monolayer Nb_2CCl_2 crystals, resulting in T_c values of up to 40 K. In the S-functionalized cases our calculations reveal the importance of phonon softening in understanding their superconducting properties. Finally, we predict that $Nb_3C_2S_2$ in bulk-layered and monolayer form is also superconducting, with a T_c around 30 K. Considering that Nb_2C is not superconducting in pristine form, our findings promote functionalization as a pathway towards robust superconductivity in MXenes.

1 Introduction

Layered metal carbides, nitrides, and carbon-nitrides, named MXenes in the literature, have risen among the most attractive material families in recent years. Numerous studies have been published on the use of these materials, which generally have metallic properties, in numerous technological applications such as supercapacitors[1], ion batteries[2–4], electromagnetic shielding[5,6], and other[7–10]. In addition, significant progress in synthesis of MXenes has been achieved[11], which created a positive feedback loop to the intensity of research on these materials. In particular, extraordinary developments have recently been reported regarding nanoengineering of functional groups covering both sides of the MXene layers, fostering custom-engineered layered MXene crystals with desired functionalities[12,13].

For instance, by using substitution and elimination reactions in molten inorganic salts, Kamysbayev *et al.* have synthesized high-quality layered MXene crystals that only differ by their functional group, such as Nb_2CCl_2 and Nb_2CS_2[14]. For these crystalline layered structures, they demonstrated the strong influence of the functional group on the electronic properties through electrical characterization. They observed a distinctive superconducting transition for Nb_2CT_2 (with T = Cl, S, Se) crystals with superconducting critical temperatures (T_c) amounting to $\sim$6, $\sim$6.5, and $\sim$4.5 K for Nb_2CCl_2, Nb_2CS_2, and Nb_2CSe_2, respectively. Wang *et al.* recently confirmed the findings for Nb_2CCl_2, obtaining a T_c of 5.2 K[15].

In fact, bare monolayer Nb_2C does not show a superconducting transition, as demonstrated experimentally in these same studies, and predicted from first-principles calculations in our prior work[16]. While functionalization with hydrogen strongly enhances the T_c of molybdenum- and tungsten-based MXenes – up to 32 K predicted through first-principles calculations – the T_c of hydrogenated Nb_2C remains limited to 0.8–2.9 K (depending on the hydrogen positions)[17].

Overall, the strong influence of the functional groups on superconductivity in MXenes is rather clear. However, the main physical mechanism responsible for inducing superconductivity upon functionalization is still not completely elucidated, beyond the first first-principles calculations reported for bulk Nb_2CCl_2[15] and Nb_2CS_2 in two-dimensional (2D) form[18]. Therefore, in this work we have thoroughly investigated and compared the superconducting properties of the recently synthesized Nb_2CCl_2, Nb_2CS_2, and Nb_2CSe_x crystals, in both their bulk and monolayer form.

In contrast with the available experimental results, our calculations indicate the absence of superconductivity in Se-based MXenes. Interestingly, the stoichiometry of these crystals in the experiment[14] deviates significantly from the ideal unit formula Nb_2CSe_2 considered in our calculations. Therefore, we will focus here mostly on the potential of functionalization with chlorine and sulfur to induce superconductivity in niobium-carbide MXenes, considering Nb_2CT_2 (with T = Cl or S) in bulk-layered and monolayer form, as well as $Nb_3C_2T_2$ (with T = Cl or S), depicted in Fig. 1.

2 Methodology

The calculations were performed using the density functional theory (DFT), as implemented within the ABINIT code[19,20]. The Perdew–Burke–Ernzerhof (PBE) type[21] Hartwigsen–Goedecker–Hutter (HGH) pseudopotentials[22] are adopted for this purpose. The valence electron configuration of the used pseudopotentials for Nb, C, Cl, and S are $4s^24p^64d^45s^1$, $2s^22p^2$, $3s^23p^5$, and $3s^23p^4$, respectively. For all the calculations, the energy cutoff value of 50 Ha for the plane-wave basis was used. The k-point grids of 24×24×4 and 24×24×1 are employed for the bulk and 2D MX-

(a) Nb$_2$CT$_2$ Bulk

(b) Nb$_2$CT$_2$ 2D

(c) Nb$_3$C$_2$T$_2$ 2D

Nb

Cl/S

C

$\hat{z}$
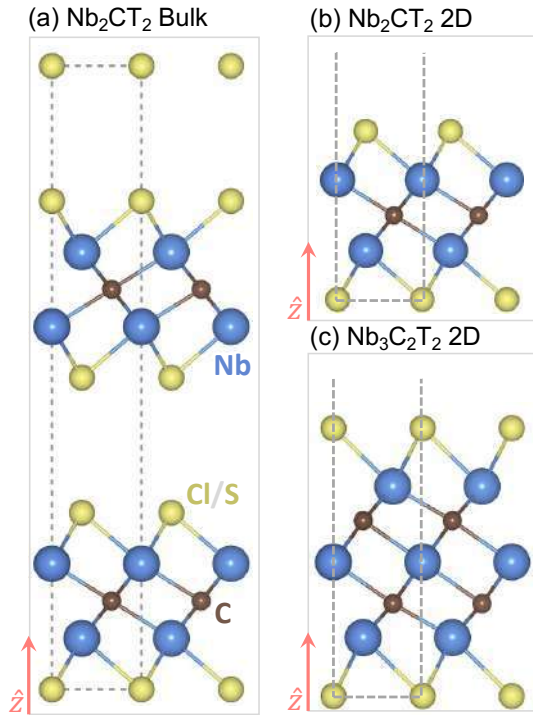
Fig. 1 Crystal structures of (a) bulk-layered and (b) monolayer (2D) Nb$_2$CT_2, and (c) monolayer Nb$_3$C$_2$$T_2$, with T = Cl or S.

ene crystals, respectively. The crystal structures were relaxed so all force components were below 10^{-6} Ha/bohr for each atom. The used vacuum space to model the 2D structures was at least 15 Å.

To calculate phonon dispersions and the electron-phonon (*e-ph*) coupling we used density functional perturbation theory (DFPT) as implemented in ABINIT[23], using 8×8×1 and 12×12×1 phononic *q*-point grids. For the smearing of the electronic occupations around the Fermi level we used the Methfessel-Paxton method. To characterize the superconducting state we then relied on isotropic Migdal-Eliashberg theory, a quantitatively accurate extension to the Bardeen–Cooper–Schrieffer (BCS) theory for phonon-mediated superconductivity[24–26]. We evaluated the superconducting T_c in different cases using the Allen–Dynes formula[27–29]. Here, the average screened Coulomb repulsion between Cooper-pair electrons (μ^*) is determined from the comparison to the available experimental measurements[14], within the range of expected values for transition metal-based compounds[30].

3   Results

In order to investigate the layered crystals as synthesized by Kamysbayev *et al.*, we have first studied the structural properties, with the reported experimental structures as the starting point. Our results for the in-plane lattice parameters are in very good agreement with the experimental values, as seen in Table 1. However, the deviation for the out-of-plane lattice constant, i.e. in the direction along which the MXene layers are stacked, is around 10% for all the calculated layered MXene crystals. Therefore, the
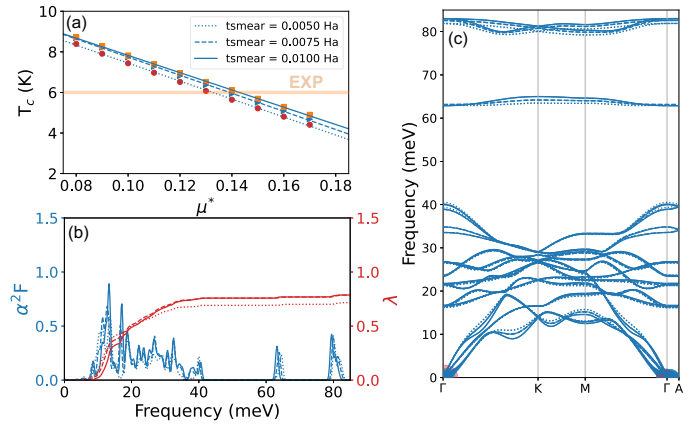

Fig. 2 Superconducting properties of bulk-layered Nb$_2$CCl$_2$. (a) The dependence of the superconducting transition temperature, T_c, on the Coulomb pseudopotential μ^*. (b) The Eliashberg function, $\alpha^2 F$, and *e-ph* constant, λ. (c) The phonon dispersion along with the *e-ph* coupling strength, indicated by the size of the dots (red = 50×blue). The solid, dashed and dotted lines in all panels represent results obtained with different electronic smearing values, *tsmear*.

van der Waals (vdW) interaction as proposed by Grimme, based on the addition of a semi-empirical dispersion potential (DFT-D2 and DFT-D3)[31,32], as well as the Becke-Jonshon method[33], were tested, and improved agreement with the experimental values was reached. However, all the phonon dispersion calculation tests with inclusion of vdW interaction resulted in imaginary frequencies, which hampered the calculation of the *e-ph* coupling and the superconducting properties. Therefore, we proceeded without inclusion of vdW corrections in the calculations presented here. To investigate interlayer interaction further, we calculated the exfoliation energies of different functionalized bulk-layered MXenes. We obtained values of $\sim$ 1 meV/atom or less (see Supplementary Material), indicating that the layers are only weakly coupled.

3.1   Chlorine-functionalized Nb$_2$C

3.1.1   Bulk-layered structure

It is a well-known fact that parameters such as the Coulomb pseudopotential (μ^*), describing the effective electron-electron repulsion within the Cooper pairs, and the electronic smearing factor used in the DFPT calculations (*tsmear*), may have a strong influence on the superconducting properties. Therefore, we per-

Table 1 Calculated and experimental structural parameters of the considered MXene crystals. TW, EXPI, and EXPII correspond to the results of this work, experimental values reported in Ref.[14], and experimental values reported in Ref.[15], respectively.

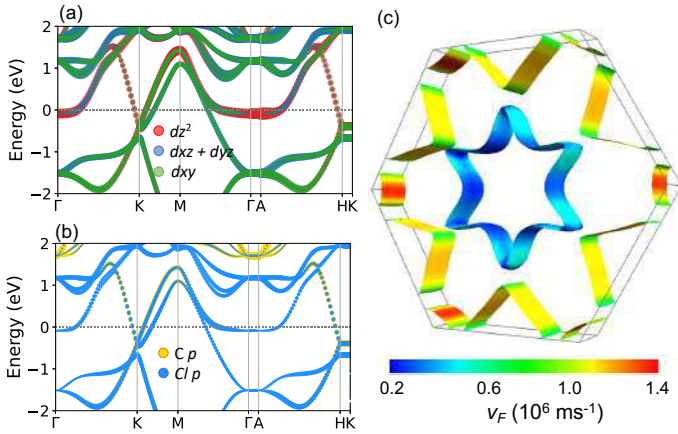| MXene	Ref.	Symmetry	a_0 (Å)	c_0 (Å)
Nb$_2$CCl$_2$	TW	$P6_3/mmc$	3.353	19.947
Nb$_2$CCl$_2$	EXPI	$P6_3/mmc$	3.311	17.656
Nb$_2$CCl$_2$	EXPII	$P6_3/mmc$	3.162	17.655
Nb$_2$CS$_2$	TW	$P6_3/mmc$	3.281	20.018
Nb$_2$CS$_2$	EXPI	$P6_3/mmc$	3.265	18.388
Nb$_2$CSe$_2$	TW	$P6_3/mmc$	3.326	21.116
Nb$_2$CSe$_2$	EXPI	$P6_3/mmc$	3.282	23.296

Fig. 3 Electronic properties of bulk-layered Nb_2CCl_2. (a)-(b) Angular momentum-resolved electronic band structures, with the Fermi level at zero. Here, the red, blue, green, yellow and blue solid circles represent the Nb d_{z^2}, Nb $d_{xz} + d_{yz}$, Nb d_{xy}, C p, and Cl p contribution respectively. (c) The Fermi surface, together with the Fermi velocities.

Fig. 4 The effect of gating on the superconducting properties of bulk-layered Nb_2CCl_2. (a) T_c along with the electronic density of states, as a function of the electronic energy level. (b) Carrier doping levels with Fermi level shift - negative values correspond to hole doping. (c) Eliashberg function, α^2F, and the electron-phonon coupling constant, λ, for different values of the gating-shifted Fermi level. (d) Fermi surface, along with Fermi velocities, for the Fermi level shifted by gating to ~80 meV below the intrinsic value.

formed a systematic analysis of the influence of these values. For Nb_2CCl_2, we found the system to be dynamically stable, with hardly any effect of the *tsmear* value on the the electronic density of states (DOS) around the Fermi level (4.07, 3.51, and 3.39 states/eV per unit cell, for *tsmear* = 0.0100 Ha, 0.0075 Ha, and 0.0050 Ha respectively), the phonon dispersion, or the corresponding *e-ph* coupling. Therefore, the found superconducting T_c values are nearly identical for all these cases, as seen in Fig. 2(a). The obtained T_c values are furthermore in good agreement with the experimentally measured value of $\sim$ 6.0 K, as shown in Fig. 2(a), for a μ^* around 0.13, which is precisely the expected value for a transition metal-based superconductor[30]. The calculated Eliashberg spectral function of the *e-ph* coupling and resulting *e-ph* coupling constant, reaching a maximal value of $\lambda = 0.79$, are displayed in Fig. 2(b) *. The phonon dispersion shown in Fig. 2(c) clearly shows the stability of the material, even for the lowest *tsmear* values. The dominant contribution of the acoustic and low-frequency optical modes on the *e-ph* interaction and the resulting T_c value is clearly visible. The agreement between the experiment and the presented isotropic Eliashberg calculations is very good, clearly demonstrating the phonon-mediated nature of the observed superconductivity in Nb_2CCl_2.

To further characterize the origin of the superconducting state in Nb_2CCl_2, we also investigated the electronic structure. Fig. 3(a-b) shows the angular momentum-resolved electronic band structure of bulk Nb_2CCl_2. The Nb d_{z^2} and Nb d_{xy} orbitals dominate the states near the Fermi level. The $d_{xz} + d_{yz}$ state also contributes notably in the vicinity of the Γ and K high-symmetry points. There are also limited contributions of C and Cl p states, as shown in Fig. 3(b). The resulting Fermi surface, shown in Fig. 3(c) along with the Fermi velocities, consists of three distinct types of sheets: (i) a hexagonal sheet centered around Γ, stemming from a mixture of Nb d states (d_{z^2} mainly), (ii) six quasi-
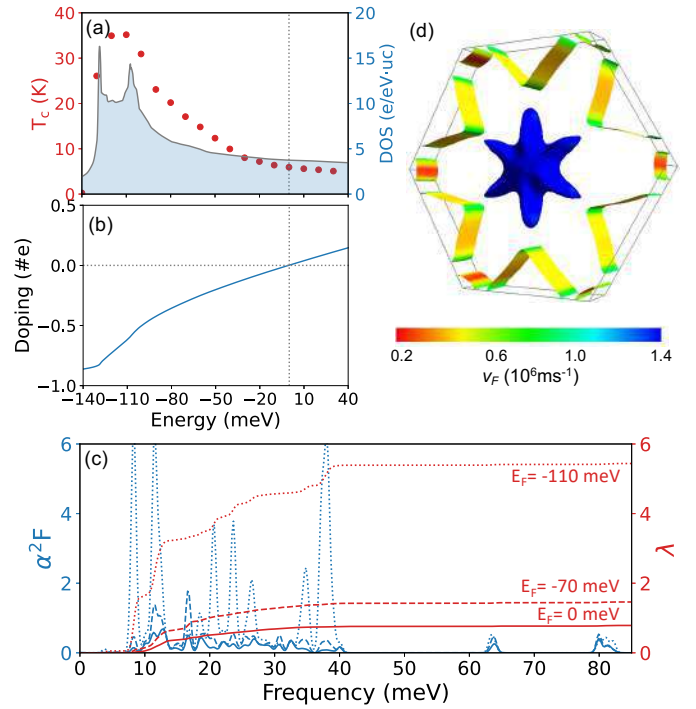
circular sheets around the K points consisting of a mixture of Nb d_{z^2} and d_{xy} states, and (iii) six rhombus-shaped sheets centered around the M points, mainly due to Nb d_{xy} states. The Γ-centered sheet has relatively low Fermi velocities, while the sheets centered around the K points harbor the highest Fermi velocities.

3.1.2 Two-dimensional structure

At this point, we recall that entirely two-dimensional counterparts of these bulk layered MXenes can also be experimentally fabricated. Our calculations show the layer-by-layer separation energies of these crystals to be as low as 1 meV/atom – as shown in the Supplementary Material – especially due to their surface functional groups. Therefore, we also analyzed the properties of two-dimensional Nb_2CCl_2 crystals depicted in Fig. 1(b). Our calculations show the superconducting properties of bulk and monolayer cases to be rather similar. As shown in the Supplementary Material, the calculated vibrational properties and *e-ph* coupling values in a monolayer are almost the same as the ones obtained for the bulk-layered crystal. The total *e-ph* coupling constant λ amounts to 0.9, which is slightly higher than the one obtained for the bulk case (0.8). As a result of a slight increase in both λ and the electron density of states at the Fermi level, the calculated T_c value of monolayer Nb_2CCl_2 is enhanced to 10 K (using the same $\mu^* = 0.13$), compared to 6 K for the bulk-layered case.

*For comparison, Ref. 15 reported a lower calculated *e-ph* coupling constant ($\lambda = 0.63$) and lower T_c (5.2 K), using a reduced μ^* value (0.1).

3.1.3 Enhancing superconductivity by gating

Both the bulk-layered and the monolayer forms of Nb_2CCl_2 harbor a distinctly flat electronic dispersion around the Γ and A points, right below the Fermi level (see Fig. 3(a–b), and the Supplementary Material, respectively). This evokes the possibility of tailoring the superconducting properties of this material using an applied gate voltage. Therefore, we performed electron-phonon coupling and T_c calculations for correspondingly shifted Fermi level values, considering both electron- and hole-type gating. Fig. 4(a) shows the obtained T_c values (using $\mu^* = 0.13$) of bulk-layered Nb_2CCl_2 as a function of the Fermi level shifted by gating. The T_c increases up to 35 K with the shift of Fermi level coinciding with the flat dispersion. In Fig. 4(b), the Fermi level shift is related to the number of removed or added electrons, as calculated from the integrated density of states. This analysis shows that a feasible doping of ~ 0.6 holes per 10-atom unit cell, corresponding to a Fermi level shift of -120 meV, is sufficient to reach the highest T_c value of 35 K for bulk-layered Nb_2CCl_2.

As seen in Fig. 4(c), the increase in the density of states results in enhanced *e-ph* coupling to both acoustic and optical vibrations within the 0–40 meV vibrational energy range. This enhanced interaction arises once the Fermi level is shifted to ~ 80 meV below the original one, and paves the way for T_c above 20 K. The density of states enhancement is mainly provided by the increase in surface area of the predicted six-pointed star-shaped Fermi sheet centered around Γ, as seen in Fig. 4(d). In line with our findings for the intrinsic case, a similar Fermi shift boosts the T_c of monolayer Nb_2CCl_2 up to 40 K (see the Supplementary Material). Therefore, these results convincingly demonstrate the prospect of using gate voltages to significantly engineer the T_c of this functionalized MXene. Moreover, this is one further advantage brought by functionalization, as superconductivity in pure Nb_2C did not exhibit sensitivity to gating[17].

3.1.4 Enhancing superconductivity by strain

Recently, feasible fabrication of wrinkles and buckles, and conformable patterns, next to the use of piezo-electric substrates, have been demonstrated to produce controllable tensile strain in layered materials[34]. The use of such mechanical deformation to engineer superconducting properties of 2D materials has been amply demonstrated. Generally, tensile strain enhances the superconducting T_c of 2D materials, as e.g. shown for MgB_2[35,36], while compressive strain weakens superconductivity, as demonstrated for MgB_2[35,36] and $NbSe_2$[37]. Therefore, we investigated the possibility of achieving enhanced T_c values in functionalized Nb-based MXenes under the influence of applied strain. Our electronic band structure calculations show a gradual shift of the Nb-d_{z^2}, Nb-d_{xy}, and Cl-p states towards the Fermi level with increasing strain values, as shown in Fig. 5(a). Due to their flat dispersion within a sizeable portion of the Brillouin zone, this strain-driven shift leads to elevated DOS values at E_F, reaching a maximum at 0.75% tensile strain, where the flat band portion crosses E_F. This leads to a λ value enhanced above 2 at this strain level, as depicted in Fig. 5(b), and a corresponding T_c of 26 K – more than twice higher than the equilibrium value (10 K). This clearly demonstrates the potential of applying tensile strain to
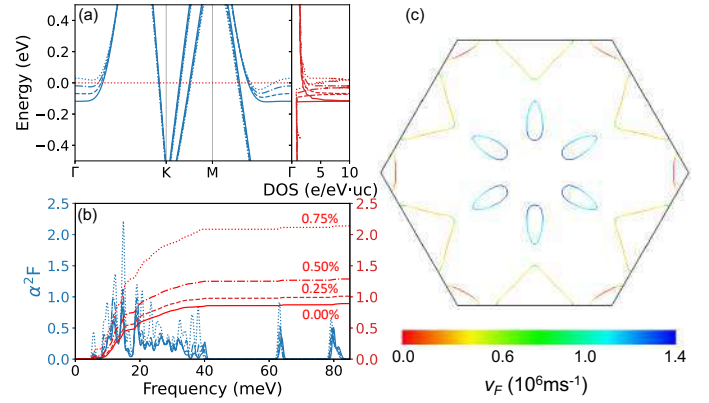

Fig. 5 The calculated (a) electronic band structure, and (b) Eliashberg function, $\alpha^2 F$, and the electron-phonon coupling constant, λ, for two-dimensional Nb_2CCl_2 under applied tensile strain. The Fermi surface corresponding to the case with 0.75% applied tensile strain is presented in panel (c).

Cl-functionalized Nb_2C to enhance and tailor its superconducting properties. Similar to the effect of gating, discussed in the preceding section, tensile strain results in an increase in the surface area of the predicted six-fold symmetric Fermi sheets centered around Γ, shown in Fig. 5(c), driving the remarkable increase in λ and T_c.

3.2 Sulfur-functionalized Nb_2C

3.2.1 Bulk-layered structure

Unlike Nb_2CCl_2, the calculated *e-ph* coupling for the S-functionalized crystal is highly sensitive to the used electronic smearing value. Computational parameters similar to the ones used for Nb_2CCl_2 (*tsmear* = 0.075 Ha and $\mu^* = 0.13$) result in a T_c value of 2.0 K, whereas the experimentally measured value is 6.5 K, as indicated in Fig. 6(d). Lowering the smearing value has a significant effect on the *e-ph* coupling of the acoustic modes, which soften around high-symmetry point K. This phonon softening corresponds to opposite circular motion of the Nb atoms within the same layer, as shown in Fig. 6(b). It results in a strong increase in λ, as shown in Fig. 6(c). Ultimately, the structure becomes unstable at smearing values around 0.0010 Ha. The other phonon branch-resolved λ values remain nearly unchanged for all the used smearing values. The calculated *e-ph* constant and T_c are therefore highly sensitive to the used smearing value. A reasonable agreement with the experimental value is obtained for *tsmear* around 0.0015 Ha and $\mu^* = 0.11$, as shown in Fig. 6(d).

Since reduced *tsmear* values mimic the effect of a reduced electron temperature, the occurrence of a dynamical instability for the lower range of *tsmear* values, is indicative of a lattice reconstruction at low temperatures. This reconstruction is expected to mainly involve the positions of the Nb atoms, as they are responsible for the emergence of the instability. The full effect of this phonon softening, and a potential crystal structure reconstruction, is worthy of further investigation, with the inclusion of anharmonicity in the phonon spectrum[38].

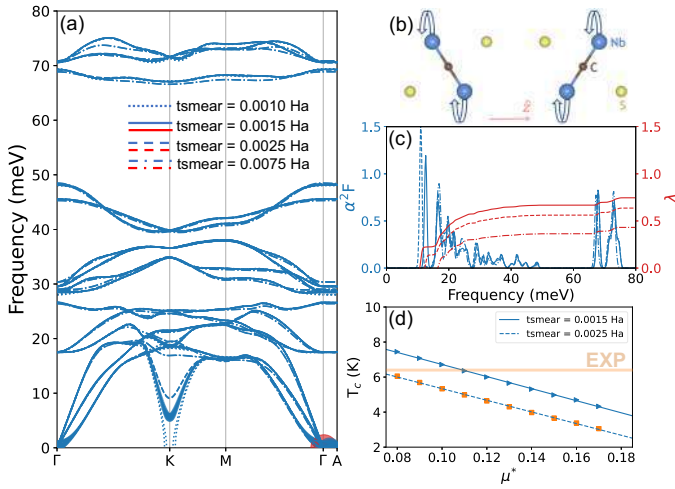The calculated angular momentum-resolved electronic band

Fig. 6 Superconducting properties of bulk-layered Nb_2CS_2. (a) The phonon dispersion, where the size of the colored circles indicates the strength of the *e-ph* coupling (red = 50×blue). (b) Atomic displacements corresponding to the soft phonon mode. (c) The Eliashberg function, $\alpha^2 F$, and *e-ph* coupling constant, λ. (d) The dependence of T_c on the Coulomb pseudopotential μ^*. The solid, dashed and dotted lines in all panels represent results obtained with different electronic smearing values, *tsmear*.

Fig. 7 Electronic properties of bulk-layered Nb_2CS_2. (a)-(b) The angular momentum-resolved electronic band structures, with the Fermi level at zero. Here, the red, blue, green, yellow and blue solid circles represent the Nb d_{z^2}, Nb $d_{xz} + d_{yz}$, Nb d_{xy}, C p, and S p contribution respectively. (c) Fermi surface together with the Fermi velocities.

structure of bulk-layered Nb_2CS_2 is shown in Fig. 7 (a) and (b). The dominant states around the Fermi level are Nb d_{z^2} and d_{xy}, similarly to the Cl-functionalized case. However, in contrast to the Cl case, there is strong hybridization between the Nb d and S p states. The corresponding bands form four types of Fermi sheets, as shown in Fig. 7(c). There are two Γ-centered nested cylindrical sheets, six elliptic sheets along the Γ-K path, and six rhombus-shaped sheets centered around the K points, which possess relatively high Fermi velocities compared to the other sheets. Consequently, this analysis clearly shows that the additional valence electron of Cl compared to S significantly affects the band structure around the Fermi level. Therefore, the electronic nature of superconductivity in these two compounds is distinctly different.

Since the Fermi surface of bulk-layered Nb_2CS_2 consists of many sheets among which some appear to be nested (e.g., between adjacent K and K' points), we investigated whether nesting drives the dynamical instability of this compound. To this end, we calculated the nesting function (see Supplementary Figure 8), showing no enhanced nesting around K compared with the rest of the Brillouin zone. Hence, Fermi surface nesting is not responsible for the phonon instability in Nb_2CS_2, in line with earlier reports, where nesting was shown to not relate directly to the emergence of charge density waves in a selection of transition-metal compounds [39].

3.2.2 Two-dimensional structure

In line with the Cl-functionalized case, the electronic properties of monolayer Nb_2CS_2 are very similar to the bulk-layered case – see Fig. 8(a). These results clearly reveal that the chemical bonding within the layers is nearly unaffected by the stacking order, for both considered functiona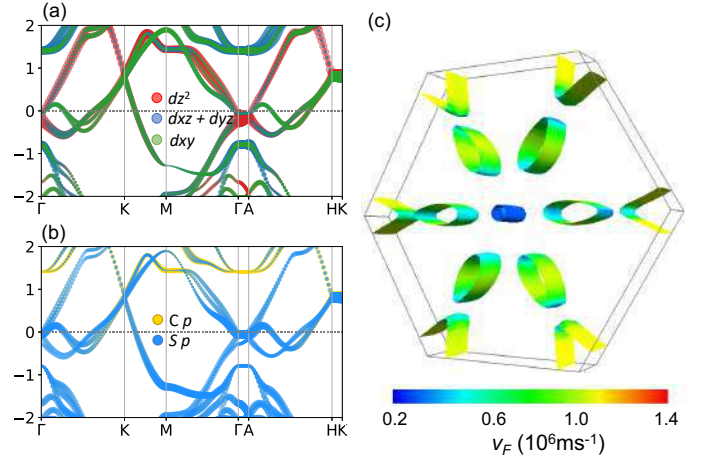lization types. However, in the S-functionalized case, the vibrational properties differ notably between the bulk-layered and monolayer cases, in that the marked phonon softening found in the former is suppressed in the latter – as shown in Fig. 8(b). Other features of the vibrational spectrum are nearly identical. Only a slight softening near the high symmetry point K is present in the monolayer case, even for *tsmear* values as low as 0.0010 Ha. This indicates that the monolayer form of Nb_2CS_2 is more dynamically stable than the bulk-layered one. The calculated Eliashberg function and integrated electron-phonon coupling constant, depicted in Fig. 8(c), are slightly different from the bulk case. In particular, the strong coupling of the acoustic modes up to 20 meV results in enhanced T_c values, 10 K and 12 K for *tsmear* = 0.0015 and 0.0010 Ha, respectively. These T_c values are almost twice higher than those obtained for the bulk case [†].

3.2.3 Enhancing superconductivity by strain

As the electronic structure of monolayer Nb_2CS_2 lacks a peak in the DOS in the proximity of the Fermi level, contrary to the Cl-functionalized case, gating does not provide a viable route towards enhanced superconducting properties in this compound. However, strain-based engineering is still worth investigating due to its potential influence on the phonons and the *e-ph* coupling. Unfortunately, our results presented in detail in the Supplementary Material reveal that tensile strain only leads to a slight enhancement of the superconducting T_c, while compressive strain results in a signification reduction of T_c. On a positive note, these results indicate that superconductivity in this compound is robust up to at least 4% of applied tensile strain.

[†] A recent *ab initio* study by Wang *et al.* reported a T_c of only 4.5 K for the monolayer case [18], in spite of the presence of significant phonon softening, absent in our result. The discrepancy with our result of an enhanced T_c may stem from the rather sparse 12^2 and 6^2 k- and q-point grids used in their calculations, as opposed to our denser 24^2 and 12^2 k- and q-point grids.
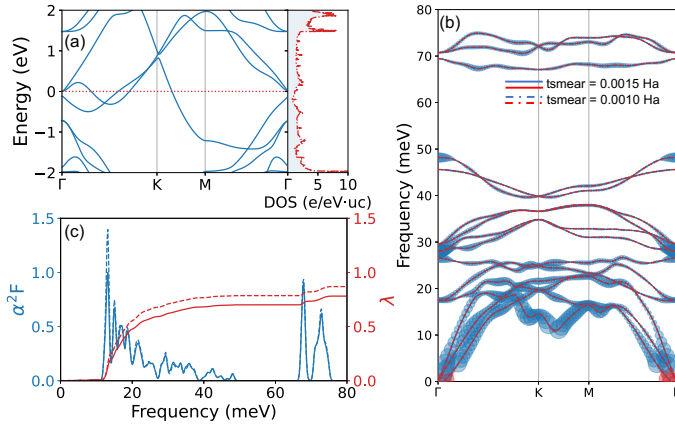
Fig. 8 Electronic and superconducting properties of monolayer Nb_2CS_2. (a) Electronic band structure, with the Fermi level at zero, and density of states. (b) Phonon dispersion along with the *e-ph* coupling strength. The size of colored circles shows the strength of the *e-ph* coupling (red = 50×blue). (c) Eliashberg function, α^2F, and *e-ph* coupling constant, λ. Here, the dashed and solid lines represent the results obtained with *tsmear* values of 0.0010 and 0.0015 Ha, respectively.
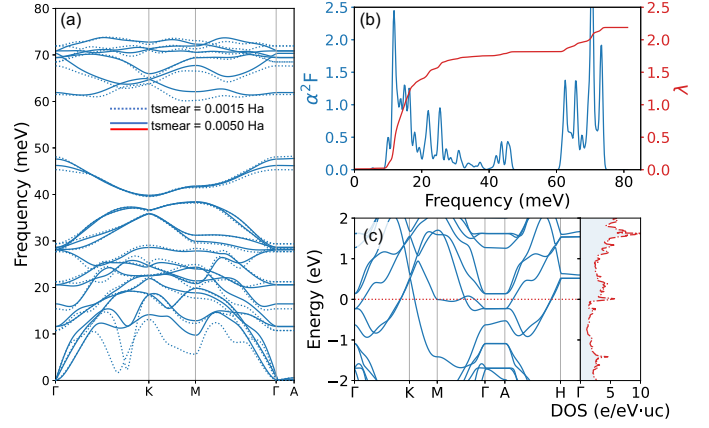

Fig. 9 Electronic and superconducting properties of bulk-layered $Nb_3C_2S_2$. (a) Phonon dispersion, where the dashed and solid lines represent the results obtained with *tsmear* values of 0.0015 and 0.0050 Ha, respectively. (b) Eliashberg function, α^2F, and *e-ph* coupling constant, λ. (c) Electronic band structure, with the Fermi level at zero, and the corresponding density of states.

3.3 Selenium-functionalized Nb_2C

In addition to the Nb_2CCl_2 and Nb_2CS_2 structures with experimentally measured Nb/surface-atom ratio close to 1, Nb_2CSe – having the same space symmetry, but with a Nb/Se ratio close to 2 – was also reported as superconducting with a T_c of 4.5 K[14]. Hence, we have investigated Nb_2CSe_2 using the same computational approach. As shown in the Supplementary Material, the Nb_2CSe_2 crystal is dynamically stable, but it does not show superconductivity due to the weak *e-ph* coupling. Here, the off-stoichiometric nature of the experimentally obtained Nb_2CSe crystal, which may be a compound high in Se-vacancies (potentially an ordered vacancy compound), is expected to be responsible for this apparent discrepancy between theory and experiment.

3.4 Functionalized Nb_3C_2

In order to shed more light on the potential of niobium-carbide MXenes as superconductors, we also considered $Nb_3C_2T_2$ crystals, as depicted in Fig. 1(c). In the Supplementary Material we show that pristine Nb_3C_2 in 2D form is dynamically stable, but possesses only limited superconducting capabilities, with an estimated T_c of merely 1 K. Due to computational limitations related to larger supercells, we only considered the stacking order with space group symmetry $P\bar{3}m1$ for the bulk functionalized structures. This corresponds to AB layer stacking resulting from a single layer in the computational unit cell. The Cl-functionalized case was found to be dynamically unstable, as shown in the Supplementary Material. On the other hand, the calculated phonon dispersion of the S-functionalized case indicates general dynamical stability, albeit in presence of a soft phonon mode along the Γ–K path for reduced *tsmear* values, as shown in Fig. 9(a). The occurrence of this phonon softening is in line with our findings for bulk-layered Nb_2CS_2 (see Fig. 6(a)). The phonon softening in bulk-layered $Nb_3C_2S_2$ disappears for higher *tsmear* values (e.g. 0.0050 Ha), as seen in Fig. 9(a). The obtained *e-ph* coupling con-

stant, depicted in Fig. 9(b), is more than double those of the other considered functionalized niobium-carbide MXenes. The strong electron-phonon coupling, boosted by the nearly localized Nb d states around the Fermi level, shown in Fig. 9(c), gives rise to an elevated T_c of ~ 30 K.

The effect of dimensional reduction (exfoliation) on the properties of $Nb_3C_2S_2$ is similar to the Nb_2CT_2 cases. The calculated phonon dispersion for *tsmear* = 0.0050 Ha, and the corresponding *e-ph* coupling properties remain akin to the bulk-layered case, as shown in the Supplementary Material, resulting in an unchanged T_c of 30 K for monolayer $Nb_3C_2S_2$.

4 Conclusions

In this work, we set out to theoretically identify the effects of selected functionalizations on superconductivity in the otherwise not superconducting Nb_2C MXene crystal. Furthermore, we have explored the effect of dimensionality, gating and applied strain on the superconducting properties of functionalized Nb-carbide MXenes. Our first-principles calculations yield profound possible improvements in the superconducting transition temperatures, as summarized in Table 2.

The superconducting properties of Nb_2CCl_2 in bulk-layered form revealed a good agreement with the recently experimentally measured T_c of 6 K[14]. In addition, we have shown that superconductivity in Nb_2CCl_2 persists in monolayer form, even with a slightly increased T_c of ~10 K. Furthermore, the occurrence of Nb d states with a flat dispersion just below the Fermi level enables an enhancement of the T_c through gating, of up to 35 K in bulk-layered form, and even 40 K in the monolayer form. In addition, tensile strain applied to the monolayer case has a similar effect to gating, boosting T_c up to 25 K.

Our calculations also revealed a reasonable agreement with the experiment for bulk-layered Nb_2CS_2. However, the present phonon softening signals possible instability of this crystal in the pure layered structure with $P6_3/mmc$ symmetry. Further analysis including anharmonic phonon effects may elucidate the influ-

Table 2 Summary of the calculated superconducting transition temperatures of all the considered functionalized MXene compounds.

	Material	$tsmear$ (Ha)	μ^*	Strain (%)	Carrier doping (#e/u.c.)	λ	T_c (K)
Bulk	Nb_2CCl_2	0.0075	0.13	-	-	0.78	6.0
Bulk	Nb_2CCl_2	0.0075	0.13	-	-0.16	1.00	10.0
Bulk	Nb_2CCl_2	0.0075	0.13	-	-0.36	1.75	20.0
Bulk	Nb_2CCl_2	0.0075	0.13	-	-0.62	5.44	35.0
2D	Nb_2CCl_2	0.0075	0.13	-	-	0.89	10.0
2D	Nb_2CCl_2	0.0075	0.13	0.25	-	1.01	11.8
2D	Nb_2CCl_2	0.0075	0.13	0.50	-	1.29	16.4
2D	Nb_2CCl_2	0.0075	0.13	0.75	-	2.14	25.6
2D	Nb_2CCl_2	0.0075	0.13	-	-0.15	1.46	18.7
2D	Nb_2CCl_2	0.0075	0.13	-	-0.30	6.08	29.4
Bulk	Nb_2CS_2	0.0015	0.11	-	-	0.74	6.5
2D	Nb_2CS_2	0.0015	0.11	-	-	0.87	12.1
2D	Nb_2CS_2	0.0015	0.11	2.00	-	0.94	12.2
2D	Nb_2CS_2	0.0015	0.11	4.00	-	1.84	12.6
Bulk	Nb_2CSe_2	0.0015	0.11	-	-	0.22	0.00
Bulk	$Nb_3C_2S_2$	0.0050	0.11	-	-	2.24	34.8
2D	$Nb_3C_2S_2$	0.0050	0.11	-	-	1.72	29.6

ence of a possible lattice reconstruction on the superconducting properties of this crystal. On the other hand, our analysis of the monolayer form of Nb_2CS_2 shows that the phonon softening practically disappears, and that the expected T_c (12 K) is almost twice as high as the measured T_c of its bulk counterpart (~ 6.5 K)[14]. Also, both phonons and superconducting properties of monolayer Nb_2CS_2 are robust under up to 4% applied tensile strain.

Our calculations for functionalized Nb_3C_2 crystals yielded quite surprising results. First of all, we find that Cl functionalization renders this crystal dynamically unstable. Contrarily, both bulk-layered and two-dimensional $Nb_3C_2S_2$ crystals are stable (albeit showing a similar phonon softening as in bulk Nb_2CS_2) and superconducting with elevated T_c values of ~ 30 K.

Overall, our extensive first-principles exploration clearly demonstrates the potential of surface functionalization to induce superconductivity in MXenes which are not superconducting in pristine form, with critical temperatures that can be strongly enhanced through gating, owing to the presence of quasi-localized electronic states. With further stacking degrees of freedom, as well as possibilities for tailoring the positions of functional atoms and groups inside an extended stack, our findings support the promise of engineered functionalization towards robust superconductivity in MXenes.

Acknowledgements

Notes and references

1 Y. Xia, T. S. Mathis, M.-Q. Zhao, B. Anasori, A. Dang, Z. Zhou, H. Cho, Y. Gogotsi and S. Yang, *Nature*, 2018, **557**, 409–412.

2 C. J. Zhang, S.-H. Park, A. Seral-Ascaso, S. Barwich, N. McEvoy, C. S. Boland, J. N. Coleman, Y. Gogotsi and V. Nicolosi, *Nature Communications*, 2019, **10**, 849.

3 E. M. D. Siriwardane, I. Demiroglu, C. Sevik, F. M. Peeters and D. Çakır, *The Journal of Physical Chemistry C*, 2020, **124**, 21293–21304.

4 U. Yorulmaz, İ. Demiroğlu, D. Çakir, O. Gülseren and C. Sevik, *Journal of Physics: Energy*, 2020, **2**, 032006.

5 F. Shahzad, M. Alhabeb, C. B. Hatter, B. Anasori, S. M. Hong, C. M. Koo and Y. Gogotsi, *Science*, 2016, **353**, 1137–1140.

6 Z. Kandemir, E. Torun, F. Paleari, C. Yelgel and C. Sevik, *Phys. Rev. Materials*, 2022, **6**, 026001.

7 J. Guo, B. Legum, B. Anasori, K. Wang, P. Lelyukh, Y. Gogotsi and C. A. Randall, *Advanced Materials*, 2018, **30**, 1801846.

8 M. Dadashi Firouzjaei, M. Karimiziarani, H. Moradkhani, M. Elliott and B. Anasori, *Materials Today Advances*, 2022, **13**, 100202.

9 Y. Gogotsi and B. Anasori, *ACS Nano*, 2019, **13**, 8491–8494.

10 M. Khazaei, V. Wang, C. Sevik, A. Ranjbar, M. Arai and S. Yunoki, *Phys. Rev. Materials*, 2018, **2**, 074002.

11 M. Naguib, M. W. Barsoum and Y. Gogotsi, *Advanced Materials*, 2021, **33**, 2103393.

12 R. Ibragimova, P. Erhart, P. Rinke and H.-P. Komsa, *The Journal of Physical Chemistry Letters*, 2021, **12**, 2377–2384.

13 C. Wang, S. Chen and L. Song, *Advanced Functional Materials*, 2020, **30**, 2000869.

14 V. Kamysbayev, A. S. Filatov, H. Hu, X. Rui, F. Lagunas, D. Wang, R. F. Klie and D. V. Talapin, *Science*, 2020, **369**, 979–983.

15 K. Wang, H. Jin, H. Li, Z. Mao, L. Tang, D. Huang, J.-H. Liao and J. Zhang, *Surfaces and Interfaces*, 2022, **29**, 101711.

16 J. Bekaert, C. Sevik and M. V. Milošević, *Nanoscale*, 2020, **12**,

17354–17361.

17 J. Bekaert, C. Sevik and M. V. Milošević, *Nanoscale*, 2022, **14**, 9918–9924.

18 S.-Y. Wang, C. Pan, H. Tang, H.-Y. Wu, G.-Y. Shi, K. Cao, H. Jiang, Y.-H. Su, C. Zhang, K.-M. Ho and C.-Z. Wang, *The Journal of Physical Chemistry C*, 2022, **126**, 3727–3735.

19 X. Gonze, B. Amadon, G. Antonius, F. Arnardi, L. Baguet, J.-M. Beuken, J. Bieder, F. Bottin, J. Bouchet, E. Bousquet, N. Brouwer, F. Bruneval, G. Brunin, T. Cavignac, J.-B. Charraud, W. Chen, M. Côté, S. Cottenier, J. Denier, G. Geneste, P. Ghosez, M. Giantomassi, Y. Gillet, O. Gingras, D. R. Hamann, G. Hautier, X. He, N. Helbig, N. Holzwarth, Y. Jia, F. Jollet, W. Lafargue-Dit-Hauret, K. Lejaeghere, M. A. L. Marques, A. Martin, C. Martins, H. P. C. Miranda, F. Naccarato, K. Persson, G. Petretto, V. Planes, Y. Pouillon, S. Prokhorenko, F. Ricci, G.-M. Rignanese, A. H. Romero, M. M. Schmitt, M. Torrent, M. J. van Setten, B. V. Troeye, M. J. Verstraete, G. Zérah and J. W. Zwanziger, *Comput. Phys. Commun.*, 2020, **248**, 107042.

20 X. Gonze, F. Jollet, F. Abreu Araujo, D. Adams, B. Amadon, T. Applencourt, C. Audouze, J.-M. Beuken, J. Bieder, A. Bokhanchuk, E. Bousquet, F. Bruneval, D. Caliste, M. Côté, F. Dahm, F. Da Pieve, M. Delaveau, M. Di Gennaro, B. Dorado, C. Espejo, G. Geneste, L. Genovese, A. Gerossier, M. Giantomassi, Y. Gillet, D. Hamann, L. He, G. Jomard, J. Laflamme Janssen, S. Le Roux, A. Levitt, A. Lherbier, F. Liu, I. Lukačević, A. Martin, C. Martins, M. Oliveira, S. Poncé, Y. Pouillon, T. Rangel, G.-M. Rignanese, A. Romero, B. Rousseau, O. Rubel, A. Shukri, M. Stankovski, M. Torrent, M. Van Setten, B. Van Troeye, M. Verstraete, D. Waroquiers, J. Wiktor, B. Xu, A. Zhou and J. Zwanziger, *Comput. Phys. Commun.*, 2016, **205**, 106–131.

21 J. P. Perdew, K. Burke and M. Ernzerhof, *Phys. Rev. Lett.*, 1996, **77**, 3865–3868.

22 C. Hartwigsen, S. Goedecker and J. Hutter, *Phys. Rev. B*, 1998, **58**, 3641–3662.

23 S. Y. Savrasov and D. Y. Savrasov, *Phys. Rev. B*, 1996, **54**, 16487–16501.

24 G. M. Eliashberg, *J. Exp. Theor.*, 1960, **11**, 696.

25 G. M. Eliashberg, *J. Exp. Theor.*, 1961, **12**, 1000.

26 F. Giustino, *Rev. Mod. Phys.*, 2017, **89**, 015003.

27 W. L. McMillan, *Phys. Rev.*, 1968, **167**, 331–344.

28 P. B. Allen and R. C. Dynes, *Phys. Rev. B*, 1975, **12**, 905–922.

29 P. B. Allen and B. Mitrović, *Solid State Phys.*, 1983, **37**, 1–92.

30 G. Grimvall, *The electron-phonon interaction*, North Holland Publishing Co. (Amsterdam), 1981.

31 S. Grimme, *J. Comput. Chem.*, 2006, **27**, 1787–1799.

32 S. Grimme, J. Antony, S. Ehrlich and H. Krieg, *The Journal of Chemical Physics*, 2010, **132**, 154104.

33 A. D. Becke and E. R. Johnson, *The Journal of Chemical Physics*, 2006, **124**, 221101.

34 Z. Dai, L. Liu and Z. Zhang, *Advanced Materials*, 2019, **31**, 1805417.

35 J. Bekaert, A. Aperis, B. Partoens, P. M. Oppeneer and M. V.

Milošević, *Phys. Rev. B*, 2017, **96**, 094510.

36 J. Bekaert, M. Petrov, A. Aperis, P. M. Oppeneer and M. V. Milošević, *Phys. Rev. Lett.*, 2019, **123**, 077001.

37 C. Chen, P. Das, E. Aytan, W. Zhou, J. Horowitz, B. Satpati, A. A. Balandin, R. K. Lake and P. Wei, *ACS Applied Materials & Interfaces*, 2020, **12**, 38744–38750.

38 R. Bianco, L. Monacelli, M. Calandra, F. Mauri and I. Errea, *Phys. Rev. Lett.*, 2020, **125**, 106101.

39 M. D. Johannes and I. I. Mazin, *Phys. Rev. B*, 2008, **77**, 165135.